A 4,565-My-old record of the solar nebula field

Clara Maurel, Jérôme Gattacceca

A 4,565-Myr-old record of the solar nebula field

Clara Maurel[1]*, Jérôme Gattacceca[1]

[1]CNRS, Aix Marseille Univ, IRD, INRAE, CEREGE, Aix-en-Provence, France

*corresponding author

Email: cmaurel@cerege.fr

Author Contributions: CM: conception of the work, acquisition, analysis, interpretation of the data, manuscript writing, manuscript revision. JG: conception of the work, acquisition and interpretation of the data, manuscript revision.

Keywords: meteorite; paleomagnetism; solar nebula; magnetic field

Abstract (250 words)

Magnetic fields in protoplanetary disks are thought to play a prominent role in the formation of planetary bodies. Acting upon turbulence and angular momentum transport, they may influence the motion of solids and accretion onto the central star. By searching for the record of the solar nebula field preserved in meteorites, we aim to characterize the strength of a disk field with a spatial and temporal resolution far superior to observations of extrasolar disks. Here, we present a rock magnetic and paleomagnetic study of the andesite meteorite Erg Chech 002. This meteorite contains submicron iron grains, expected to be very reliable magnetic recorders, and carries a stable, high-coercivity magnetization. After ruling out potential sources of magnetic contamination, we show that Erg Chech 002 most likely carries an ancient thermoremanent magnetization acquired upon cooling on its parent body. Using the U-corrected Pb-Pb age of the meteorite's pyroxene as a proxy for the timing of magnetization acquisition, we estimate that Erg Chech 002 recorded a field of 60 ± 18 μT at a distance of ~2-3 astronomical units, 2.0 ± 0.3 million years after the formation of calcium-aluminum rich inclusions. This record can only be explained if Erg Chech 002 was magnetized by the field prevalent in the solar nebula. This makes Erg Chech 002's record, particularly well resolved in time and space, one of the two earliest records of the solar nebula field. Such a field intensity is consistent with stellar accretion rates observed in extrasolar protoplanetary disks.

Introduction

Protoplanetary disks may sustain magnetic fields present in their parent molecular cloud (1). These magnetic fields likely play a prominent role in the accretion of planetesimals, the first planetary bodies formed in protoplanetary disks. In particular, magnetic disk winds, can significantly contribute to enhancing angular momentum transport (2). As a consequence, magnetic fields have a direct influence on the disk accretion rate, favoring the displacement and concentration of solids needed to form planetesimals.

Numerical models accounting for these complex magnetic effects are being developed (3, 4). These models show in particular that the vertical component of the field (i.e., normal to the disk plane) can influence the disk dynamics, depending on whether it is aligned or anti-aligned with the disk's rotation vector. Within uncertainties, modeling suggests that, shortly after the onset of protoplanetary disk formation and within 3 astronomical units (au), a ~50-μT field in the "aligned" case would be needed to achieve an accretion rate of ~10^{-8} $M_\odot$ yr^{-1} (where $M_\odot$ is the stellar mass) (2). This accretion rate is typically observed for the bulk lifetime of extrasolar protoplanetary disks (5). However, a field of ~5 μT would also be compatible with such an accretion rate in the "anti-aligned" case (2). These two different, yet plausible scenarios illustrate the need for well-constrained estimates of magnetic field strengths in protoplanetary disks.

At present, astronomical observations of extrasolar protoplanetary disks do not provide substantial constraints on disk field strengths. In fact, although the intensity of magnetic fields in extrasolar disks may be probed through the observation of the Zeeman effect (i.e., the splitting of spectral lines in the presence of a magnetic field), a positive detection of a disk field has not yet been reported (6, 7). The only alternative to astronomical observations is the study of our own protoplanetary disk, the solar nebula. Meteorites that experienced the bulk of their thermal and/or aqueous alteration history within the lifetime of the solar nebula may carry the record of the solar nebula field in the form of a natural remanent magnetization (NRM) (2). The major advantage of meteorite paleomagnetism over (anticipated) astronomical observations of disk fields is the temporal and spatial resolution of the record. The cooling or crystallization epoch of the magnetic minerals contained in meteorites can sometimes be dated with high precision, anchoring the magnetic record of the solar nebula field in time. Moreover, the vast majority of meteorites come from < 10 au, whereas the most successful astronomical observations would likely only reach a resolution of tens of au given the current instrument sensitivity (8).

Paleomagnetic studies have already been conducted on chondrules from three meteorite groups and bulk rocks from nine meteorite groups, all possibly carrying a record of the solar nebula field. These studies focused on meteorites that originated from the so-called non-carbonaceous and carbonaceous reservoirs (9, 10), sampling the inner and outer regions of the solar nebula, within ~2-3 au and ~3-7 au, respectively (11, 12). Chondrules of the LL chondrite Semarkona provide the only paleointensity incompatible with zero for the non-carbonaceous reservoir (13). The most up-to-date estimate indicates that a field of 34^{+36}_{-14} μT existed 2.0 ± 0.8 Myr after the formation of calcium-aluminum rich inclusions (CAIs, the first solids to condensate in the nebula) (13, 14). This intensity is most consistent with an accretion rate of ~10^{-9} $M_\odot$ yr^{-1} (but compatible within uncertainties with a rate of ~10^{-8} $M_\odot$ yr^{-1}) in the aligned case, and most consistent with a rate of 10^{-7} $M_\odot$ yr^{-1}

in the anti-aligned case (2), with the caveat that the formation distance of Semarkona chondrules is not well constrained [> 2 au; (14)]. Four other non-zero paleointensities were obtained from chondrules and meteorites from the carbonaceous reservoir: CO chondrules (14, 15), the CV chondrite Allende (16, 17), CM chondrites (18), and the ungrouped carbonaceous chondrite WIS 91600 (19). These studies collectively indicate that, at ~3 to ~7 au, the nebula field intensity decayed from 106^{+88}_{-18} μT to 4.4 ± 2.8 μT between 2.2 ± 0.8 and ~4.0 ± 1.0 Myr after CAI formation. The oldest and highest paleointensity, derived from CO chondrules and incompatible with the accretion rates derived from Semarkona chondrule data, was interpreted as evidence for variable accretion rates caused by substructures in the disk (15).

The remaining studies interpreted their data as evidence for the absence of a substantial magnetic field in the formation region of the meteorites at the time they could acquire their NRM (20–25). In particular, these results were used to constrain the dissipation of the solar nebula to being less than ~5 Myr after CAI formation. Considering the multiple mechanisms that may temporally and spatially influence the intensity of the solar nebula field, it is necessary to get additional and more precise estimates of the nebula field strength to offer better constraints for dynamical models of planetary formation. For this, we must search for candidate meteorites that may have recorded the nebula field because their most recent cooling epoch or timing of aqueous alteration overlapped with the lifetime of the solar nebula.

Erg Chech 002 (EC002) is an ungrouped achondrite found in 2020 in the Algerian Sahara. It is an andesite, most likely originating from the primordial igneous crust of its parent body (26). Thermal modeling, constrained by radiometric dating using multiple isotopic systems—Al-Mg, U-Pb-Pb, Mn-Cr, Ar-Ar (26–31)—indicates that EC002's parent body accreted, melted and differentiated in the first 0.5 Myr after CAI formation. EC002 would have formed at shallow depth (~1 km) and cooled at a rate of ~170°C Myr^{-1} between 1200°C and 100°C, reaching temperatures < 100°C before 10 Myr after CAI formation (32). Based on the ^{17}O, ^{54}Cr and ^{148}Nd isotope composition of EC002 (26–29), it was confirmed that its parent body formed in the non-carbonaceous reservoir (9, 10), i.e., in the inner region of the solar nebula between ~2 and ~3 au (11).

The mineralogical description of EC002 indicates the presence of small metallic iron grains (26). These iron grains are ferromagnetic. As such, in the presence of a magnetic field, they could acquire a thermoremanent magnetization (TRM) upon cooling below the Curie temperature (T_c) of iron [770°C (33)] through a so-called blocking temperature range extending ~100°C below T_c (33). The U-corrected Pb-Pb age of pyroxene in EC002 indicates that the rock cooled through a temperature of 810 ± 65°C at a time of 2.0 ± 0.3 Myr after CAI formation (30). This temperature is similar within uncertainties to the Curie temperature of iron. Moreover, consistent Al-Mg, U-Pb-Pb, Mn-Cr ages confirm the absence of a major reheating event on the parent body (26–30). Only the Ar-Ar age of plagioclase, estimated at 58 ± 40 Myr after CAI, may indicate a minor reheating up to ~275°C (31, 32). These evidence collectively imply that EC002 underwent its ultimate cooling below the Curie temperature of iron 2.0 ± 0.3 Myr after CAI formation, well within the lifetime of the solar nebula. In this paper, we investigate the possibility that EC002 acquired and preserved a TRM reflecting the intensity of the solar nebula field.

Results

Rock magnetic analysis. Opaque minerals in EC002 are metal and various minerals that are non-magnetic at room temperature (troilite, chromite, ilmenite; Fig. S1). Electron probe microanalysis (EPMA) of five metal grains indicates the metal is pure iron, with < 0.17 wt.% nickel (Table S1). The meteorite was described as having a low terrestrial weathering grade (26). However, reflected light optical microscopy and compositional analyses using electron dispersive microscopy (EDS) of our samples show different types of oxides and/or oxyhydroxides, resulting from the terrestrial oxidation of metal and troilite grains (Fig. S1). These oxides are visible in rims around some large metal and troilite grains and as veins. Some of them are ferromagnetic, as revealed by magneto-optical imaging (Fig. S2). Note that the magnetic carriers capable of retaining a remanent magnetization over the age of the solar system [i.e., grains $\lesssim$ 200 nm, in the so-called single-domain or single vortex magnetic states (34, 35)] are not resolvable using EPMA or EDS, such that we cannot know the nature of the remanence carriers from compositional maps alone.

Low-field magnetic susceptibility (χ_{LF}), measured on 12 stones from 0.98 g to 6.39 g, ranges between 9.49×10^{-7} and 2.85×10^{-6} $m^3\,kg^{-1}$ (Table S2). These values match the range of other achondrite groups such as angrites and HEDs (36). The variability in susceptibility suggests a heterogeneous distribution of magnetic grains among the stones (Fig. S3A). The degree of anisotropy of susceptibility is weak (P = 2 to 8%, measured on 4 stones from 3.11 g to 5.83 g; Table S2). The shape factor of anisotropy of susceptibility shows variability among samples, ranging from prolate (T = -0.618) to oblate (T = 0.473). Finally, the frequency dependence of magnetic susceptibility [$(\chi_{976Hz} - \chi_{15616Hz})/\chi_{976Hz}$ = 4.7%, measured on 2 stones of 5.13 g and 6.39 g] indicates the presence of superparamagnetic grains with a minor contribution to the susceptibility (Table S2).

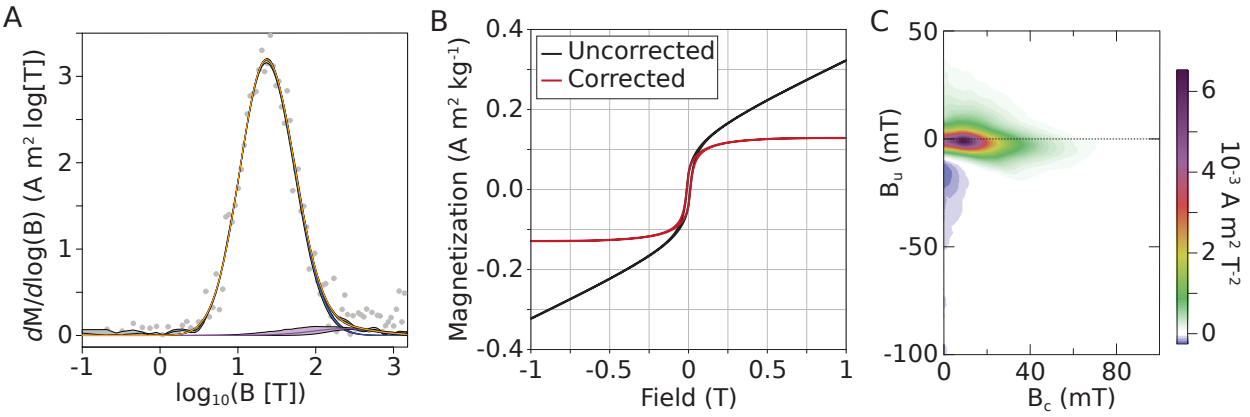

Fig. 1. Rock magnetic properties of sample S7A2-3 (74 mg). *The three panels collectively indicate that EC002 contains ferromagnetic grains in the single-domain and single-vortex magnetic states, compatible with the presence of small iron grains and/or iron oxides like magnetite formed during terrestrial alteration. (**A**) Coercivity spectrum: derivative of the isothermal remanent magnetization (IRM) acquisition curve as a function of the logarithm of the applied field. Data are shown by the gray points. The two coercivity components fitted to the data are shown by the blue and purple curves. Shaded areas show the 95% confidence intervals for each curve.*

The sum of the two coercivity distributions is shown in orange. This plot was generated using the MAX UnMix software (37). *(**B**) Hysteresis curve (before and after paramagnetic slope correction). (**C**) First-order reversal curve (FORC) diagram produced by the FORCinel software* (38).

The coercivity spectra measured for two stones exhibit a single dominant peak centered on a coercivity of 25-30 mT and representing > 90% of the saturation isothermal remanent magnetization (SIRM, the remanent magnetization remaining after applying a 3-T magnetic field; Fig. 1A; Fig. S4). The absence of high coercivity minerals is confirmed by a S_{-300} ratio (i.e., the ratio between an SIRM and a backfield IRM acquired in a 300-mT field) of -0.98 ± 0.01 (measured on 4 stones from 1.02 g to 3.23 g; Table S3). These coercivity spectra do not exclude the presence of different populations of ferromagnetic grains with undistinguishable coercivity ranges.

The mass weighted average saturation magnetization (M_s; measured on 4 samples between 74 mg and 1.56 g; Fig. 1B) is 0.42 A m^2 kg^{-1}, which corresponds approximately to 1900 ppm or 0.07 vol.% of iron metal. M_s values show a certain level of scatter among samples, indicating a heterogenous distribution of magnetic grains for samples below ~1 g (Table S3). The variability of χ_{LF} or the SIRM measured on individual stones concurs with this interpretation (Fig. S3A-B). In addition, the negative correlation of the ratio χ_{LF}/SIRM with mass (Fig. S3C) suggests that ferromagnetic grains other than iron may be more abundant in smaller samples. This may be explained by an increased content of ferromagnetic weathering products in small samples due to a larger surface area over volume ratio.

Two first-order reversal curve (FORC) diagrams display several informative features (Fig. 1C; Fig. S4): a negative signal along the B_u axis, a strong positive signal along the B_c axis centered on B_c ~ 15 mT, a slight vertical shift of the peak towards negative B_u values, and an asymmetric vertical spread around the B_c axis. The three former features are characteristic of single-domain minerals with cubic anisotropy and a low packing fraction (39). The asymmetric vertical spread suggests weak magnetostatic interactions (40). These features are compatible with the presence of single-domain and perhaps single-vortex iron grains, expected to be reliable magnetic recorders (41), but are also compatible with the presence of other magnetic carriers, such as single-domain magnetite grains formed during terrestrial oxidation.

Remanence measurement and demagnetization. We measured the NRM of twelve individual stones from 0.98 g to 6.39 g without fusion crusts (Table S4). As indicated by their characteristic curved NRM demagnetization pattern (Fig. S5) and/or their higher NRM/χ_{LF} ratios (Table S4), five out of twelve stones were contaminated by contact with a hand magnet—a practice that is unfortunately common among meteorite hunters and dealers (42). These samples were not considered for paleomagnetic analyses. We conducted alternating-field (AF) demagnetization (i.e., applying increasingly strong demagnetizing fields) of the NRM of five uncontaminated stones up to 100 mT. The NRM of these samples exhibits the same AF demagnetization pattern, with a low-coercivity (LC) component isolated between 0 and 4-6 mT depending on the sample, and a medium- to high-coercivity (MC-HC) component isolated from 8-12 mT up to 100 mT (Fig. 2A,D; Fig. S6; Table S5).

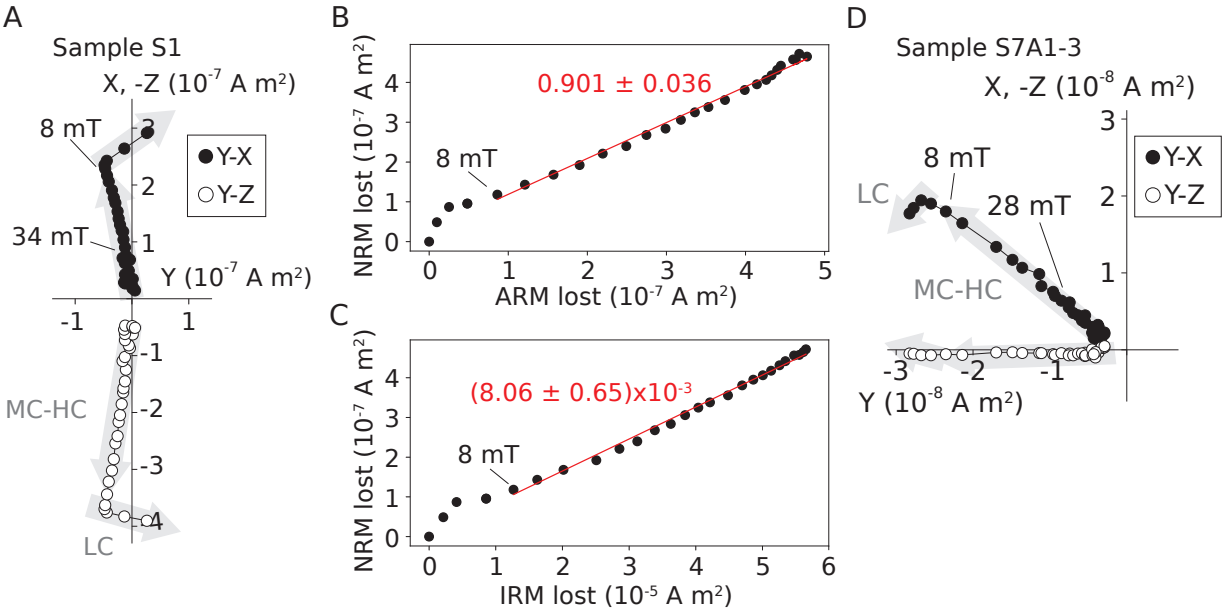

Fig. 2. Alternating-field demagnetization experiments. *(**A**) Orthogonal projection of the alternating-field (AF) demagnetization of the NRM for sample S1 (5.83 g) onto the X-Y and Y-Z planes. Arrows indicate the low coercivity (LC) and medium- to high-coercivity (MC-HC) components identified. Some demagnetization field steps are shown for reference. (**B**) NRM lost as a function of the anhysteretic remanent magnetization (ARM) lost during AF demagnetization. The best-fit line to the MC-HC component is shown in red with the corresponding slope and 2 standard error (s.e.). (**C**) NRM lost as a function of the isothermal remanent magnetization (IRM) lost during AF demagnetization. The best-fit line to the MC-HC component is shown in red with its slope and 2 s.e. (**D**) Same figure as (A) for sample S7A1-3 (102 mg), which was mutually oriented with respect to sample S7A3-3 (Fig. 3A).*

The LC component represents 10-20% of the total NRM depending on the sample (Fig. 2A,D; Fig. S6). It can most simply be explained by a viscous remanence magnetization (VRM), a remanence acquired upon resting in the geomagnetic field. To test this, we measured the VRM acquisition and decay rates (S_a and S_d, respectively) for a sample still carrying its NRM. We find a S_a/S_d ratio of 1.05, close to the value predicted for SD grains by Néel's theory (43, 44). Extrapolating the VRM acquired over 100,000 years, which is an upper limit on the terrestrial age of achondrites from the Sahara desert (45), we find that the VRM could represent 7% of the measured NRM (Fig. S7), compatible with the LC component.

The MC-HC component is well defined and origin-trending (Fig. 2A,D; Fig. S6), with a maximum angular deviation [MAD (46)] between 3.0° and 7.3° and a deviation angle [DANG (47)] between 0.8° and 6.4° (Table S5). This MC-HC component can be explained by a thermoremanent magnetization (TRM) of extraterrestrial origin carried by the iron grains, and acquired during EC002's cooling on its parent body. However, to validate this hypothesis, we must first rule out sources of magnetic contamination on Earth: exposure

to hand magnets, VRM acquisition, heating during atmospheric entry, and acquisition of a chemical remanent magnetization (CRM) by the iron oxides formed during terrestrial alteration, which would instead reflect the intensity of the geomagnetic field. Our criteria for sample selection (e.g., NRM/χ_{LF} ratio) exclude all samples that were in contact with a magnet. We also showed that a VRM could only account for a limited fraction of the NRM. Atmospheric entry thermally affects the outermost layer of the meteorite, but the temperature gradient inside the rock is very steep. Temperatures approaching the blocking temperature of iron are only reached within < 0.5 mm of the fusion crust in meteorites (48). Given that none of the cm-size stones we analyzed had fusion crust, at least the few 1/10th of mm most heated must have been removed over time, and it is very unlikely that remagnetization during atmospheric entry would be responsible for the measured NRM.

To discriminate between an extraterrestrial TRM carried by the iron grains and a terrestrial CRM carried by the iron oxides, we conducted thermal demagnetization experiments. Samples were stepwise heated between 20°C and up to 730°C in air and in a controlled atmosphere of H_2 and CO_2 (Table S6). In the controlled atmosphere experiment, the oxygen fugacity was set to 1 log(atm) below the iron-wüstite buffer (IW-1) determined for lunar basalts (49, 50). The metal and troilite contained in meteorites of similar composition to EC002 notoriously tend to alter when heated in air (51). Heating in a controlled, less oxidizing atmosphere can sometimes prevent alteration (50), though success is not guaranteed. For each condition, we measured the NRM as a function of temperature step for two samples. We also monitored potential mineralogical changes throughout the experiment by 1) imparting an anhysteretic remanent magnetization (ARM, the remanent magnetization remaining after applying a decreasing AC field and a constant DC field; here a 100-mT maximum AC field and 100-μT DC field) to a third sample after each temperature step, and 2) measuring the hysteresis properties and low-field susceptibility of a fourth sample.

In air, the NRM starts unblocking at 200°C. Beyond 240°C, the NRM exhibits a well-defined, origin-trending medium- to high-temperature (MT-HT) component with monotonic decrease in intensity (Fig. 3D-E; Table S7). Above 580°C, the intensity of the NRM reaches values < 2% of the initial NRM. A similar trend is observed in the second sample, although with a noisier signal (Fig. S8; Table S7). The intensity of the ARM applied at each step decreases by 30% at 250°C and remains constant up to 600°C. Beyond this temperature, the ARM applied is completely erased by subsequent heating (Fig. 3F). χ_{LF} remains approximately constant between 20 and 600°C, and decreases by a factor of 2 between 600°C and 700°C. M_s decreases by a factor of 3 between 20°C and 400°C before increasing back to its initial value at 500°C and decreasing again (Fig. S9).

In a controlled atmosphere, the NRM also exhibits a LT component below 240°C and a well-defined, origin-trending MT-HT component up to 730°C (Fig. 3A; Table S7). The intensity of the NRM sharply decreases between 200°C and 400°C, and then remains constant at about 5% of its initial value up to 730°C (Fig. 3B). The second sample exhibits a similar but noisier behavior (Fig. S8; Table S7). By contrast to heating in air, the ARM applied at each temperature step dramatically increases by a factor of 4.5 between 200°C and 500°C. Up to 730°C, the ARM applied is not fully erased by subsequent heating (Fig. 3C). χ_{LF} steadily increases up to a factor of 5.5 at 700°C, while M_s follows a positive trend

and increases by a factor of 9 between 200°C and 700°C (Fig. S9).

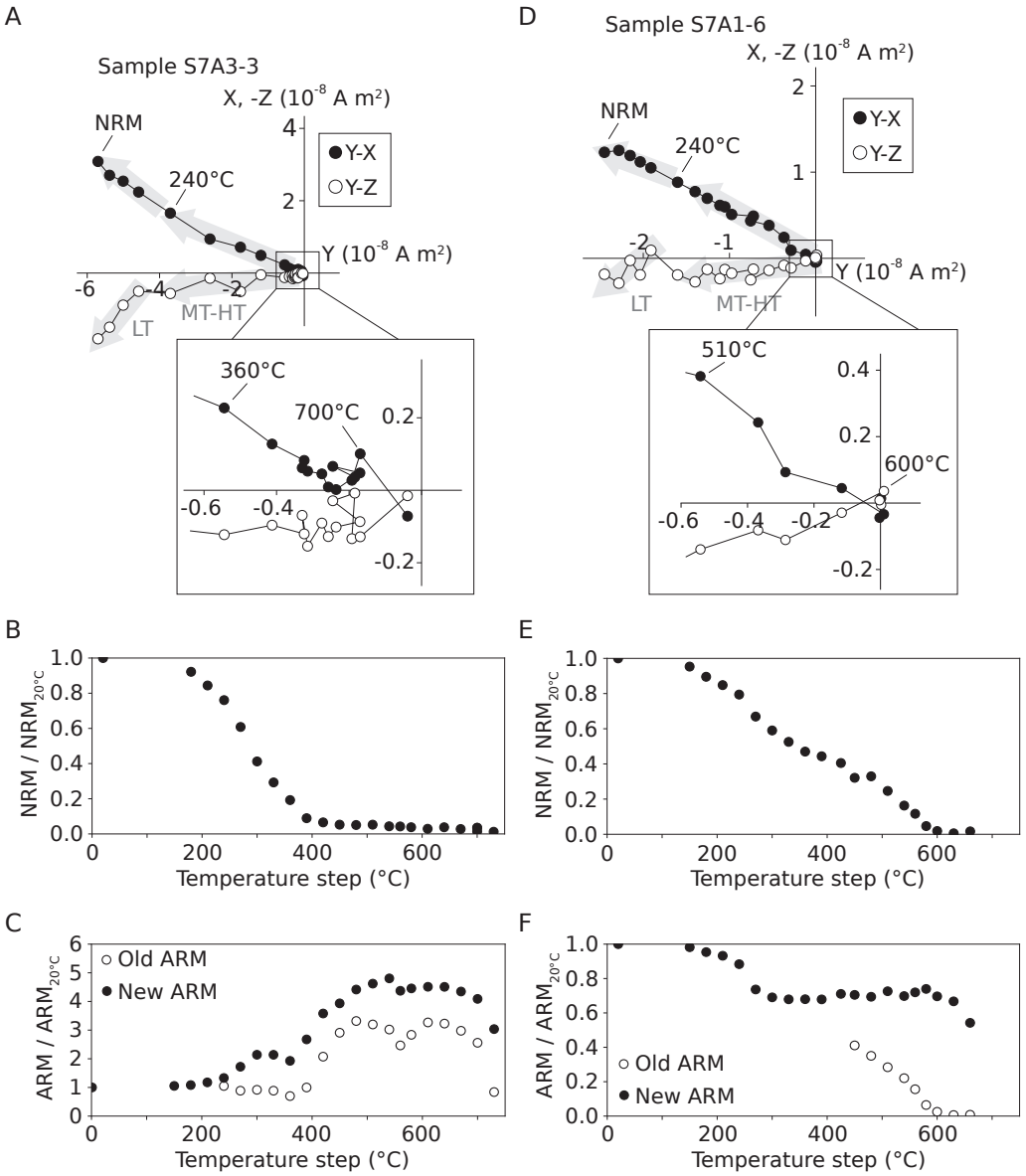

Fig. 3. Thermal demagnetization experiments conducted in air and in a controlled atmosphere. *(**A**) Orthogonal projection of the demagnetization of the NRM for sample S7A3-3 (122 mg) during heating in a controlled atmosphere. Arrows indicate the low temperature (LT) and medium- to high-temperature (MT-HT) components identified. The inset shows a zoomed-in view. Some temperature steps are shown for reference. This sample is mutually oriented with respect to S7A1-3 in Fig. 2. (**B**) NRM intensity normalized to its initial value of sample S7A3-3 heated in a controlled atmosphere as a function of temperature step. (**C**) Normalized remanence of sample S7A3-2 (255 mg) heated in a controlled atmosphere measured at each temperature step before applying an ARM (old ARM, white circles), and after applying an ARM (new ARM, black circles). (**D**) Orthogonal projection of the demagnetization of the NRM for sample S7A1-6 (100 mg) during heating in air. The sample is mutually oriented with respect to S7A3-3 in (A) and*

*S7A1-3 in Fig. 2. (**E**) Same figure as (B) for sample S7A1-6 heated in air. (**F**) Same figure as (C) for sample S7A2-5 (77 mg) heated in air.*

Nature of the remanence carriers. The thermal demagnetization data suggest that both in air and in a controlled atmosphere, massive mineralogical changes occur during heating. Despite this, the MT-HT remanence component is in reasonable directional agreement (within 10-20°; Table S5,S7) with the MC-HC component identified on an oriented companion sample that was demagnetized using AF. We attribute the observed demagnetization patterns mostly to the gradual destruction of the magnetic carriers during thermal processing, rather than to the unblocking of their remanence.

EC002 stones contain iron metal and iron oxides. Magnetite and maghemite can be found as oxidation products in weathered hot-desert meteorites (52, 53). EC002 also contains a significant amount of troilite (non-magnetic). The magnetic susceptibilities of iron metal, magnetite and maghemite are broadly similar, while the saturation magnetization of magnetite and maghemite is lower by a factor of 2 and 3, respectively, compared to iron (33). Therefore, in air, the stagnation of χ_{LF} and overall decrease of M_s, combined to the fact that any ARM applied is fully demagnetized when heating above 580°C [the Curie temperature of magnetite (33)], is compatible with a large majority of iron metal grains being replaced by magnetite. By contrast, the increase of χ_{LF}, M_s and the applied ARM in a controlled atmosphere can most simply be explained by the formation of iron metal, possibly from the partial transformation of troilite as observed in lunar samples (54, 55). This does not necessarily rule out the partial alteration of the original iron grains: we used an oxygen fugacity corresponding to IW-1 (same as lunar basalt), but this value remains unknown for EC002.

One key observation is that a fraction of the NRM remains stable in direction and intensity up to 730°C in a controlled atmosphere (Fig. 3A-B). Magnetite has a Curie temperature of 580°C and cannot explain the remanence remaining at 730°C. On the other hand, maghemite has an estimated Curie temperature of 675°C (33), although it often (but not always) inverts to weakly magnetic hematite (same Curie temperature) at lower temperatures. However, the remanence of maghemite is not inherited by hematite upon inversion (56). This implies that maghemite/hematite cannot be the carrier of the remanence remaining at 730°C. These considerations suggest that the single-domain/single-vortex iron grains present in EC002 are the most likely carriers of the MT-HT (and MC-HC) remanence component. This implies that the MT-HT (and MC-HC) component of the NRM is most likely an ancient TRM acquired during the cooling of EC002 on its parent body, and not a terrestrial CRM.

Paleointensity determination. A consequence of the mineralogical transformations observed during thermal demagnetization is that we could not use the well-established IZZI Thellier-Thellier protocol (57) to determine the paleointensity of the ancient magnetizing field (Fig. S10). As an alternative, we used the non-heating ARM and IRM normalization methods (58, 59). After conducting AF demagnetization of the NRM, we imparted the samples with an ARM (100-mT maximum AC field and 50- or 100-μT DC field) that we demagnetized using AF up to 100 mT. We then imparted the same sample with a SIRM (3-T field), that we also demagnetized up to 100 mT. The non-heating ARM and IRM normalization methods provide an estimate of the paleointensity corresponding

to a selected component of the NRM:

$$B_{\text{paleo}} = \frac{B_{\text{bias}}}{f}\frac{d\text{NRM}}{d\text{ARM}} \quad (1a)$$

$$B_{\text{paleo}} = a\frac{d\text{NRM}}{d\text{IRM}} \quad (1b)$$

In Eq. 1a-b, B_{paleo} is the paleointensity estimate, NRM, ARM, IRM are the demagnetization data for the corresponding remanences measured in the MC-HC coercivity range, and B_{bias} is the ARM DC field (Fig. 2C-D; Fig. S6). The coefficients f and a are determined empirically and depend on the nature of the magnetization and the remanence carrier. To account for the uncertainty in the values of f, a, and the slopes $d\text{NRM}/d\text{ARM}$ and $d\text{NRM}/d\text{IRM}$, we proceed by bootstrapping. We draw with replacement one value in the distribution of the slopes (Table S5) and one in the distribution of f and a to calculate B_{paleo}; this is repeated 10,000 times to obtain a 95% confidence interval on B_{paleo}. For a TRM carried by single-domain/single-vortex iron grains, the coefficients f and a follow lognormal distributions: $f = \text{lognormal}(\mu = 0.32, \sigma^2 = 0.16)$ and $a = \text{lognormal}(\mu = 8.14, \sigma^2 = 0.26)$ (60). The paleointensity estimates must also take into account the fact that the field intensity experienced by the meteorite on its parent body is the projection of the nebular field onto the spin axis of the parent body. Assuming a uniform probability distribution of planetesimal spin axis over the sphere, the paleointensities estimated from paleomagnetic data should be multiplied by a factor of 2 (13). Applying this to five stones, we find paleointensities that are very consistent using the two methods (Table S5) and average at 60 ± 18 μT (95% confidence interval).

Discussion

Our results indicate that the iron grains in EC002 most likely recorded a TRM upon cooling in a magnetic field of 60 ± 18 μT. Because the closure temperature of the U-Pb-Pb isotopic system in pyroxene is similar to the Curie temperature of iron, and because EC002 cooled through the blocking temperature range of iron (spanning ~100°C below T_c) in ~0.5 Myr based on its modeled cooling rate of ~170°C Myr^{-1} (32), the U-Pb-Pb age of EC002's pyroxene is an excellent proxy for the age of the magnetization. This implies that the TRM was acquired 2.0 ± 0.3 Myr after CAI formation, at an heliocentric distance of ~2-3 au, where EC002's parent body most likely formed.

The most common sources of magnetizing field in the early solar system are the solar nebula, a core dynamo powered by the parent planetesimal and the solar wind. According to thermal evolution models, the onset of dynamo activity on planetesimals was likely delayed by several Myr with respect to accretion (61). EC002's early magnetization epoch therefore appears incompatible with a magnetizing field powered by the advection of a liquid metallic core. Moreover, triggering and sustaining a stable core advection requires a minimum parent body diameter, estimated to be at least ~80 km (61, 62). A diameter of 20-30 km, as estimated for EC002's parent body using thermal models (32), makes the hypothesis of a dynamo activity even less likely. The estimated intensity of the field recorded by EC002 is also incompatible with the early solar wind magnetic field, whose intensity is estimated at $\lesssim$ 300 nT in the inner solar system (63). EC002's early record

and paleointensity estimate are therefore most compatible with the solar nebula being the source of the magnetizing field.

Fig. 4. Estimated nebula field intensities as a function of time after CAI formation. *The red*

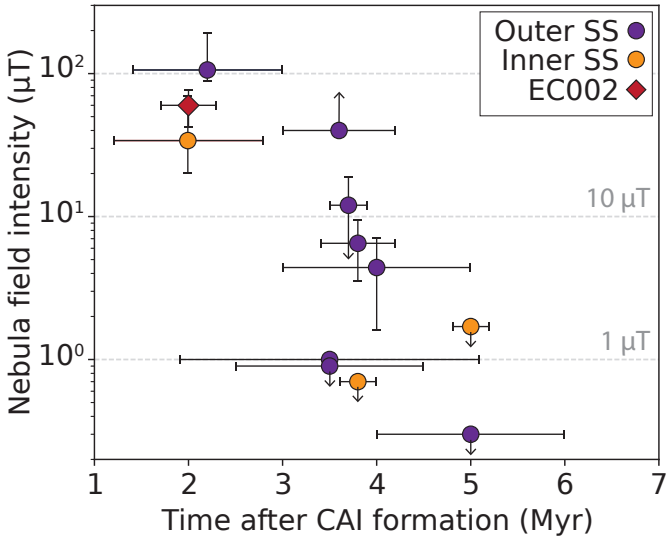

diamond corresponds to EC002's record (at ~2-3 au). Yellow circles show estimates obtained from chondrules and meteorites that formed in the inner region of the solar system (at > 2 au for Semarkona chondrules, ~2-3 au otherwise). Purple circles show estimates obtained from chondrules and meteorites that formed in the outer region of the solar system (at ~3-7 au, possibly > 7 au for Tagish Lake and WIS 91600). Data compiled from (13–25)*.*

In light of these considerations, our results provide strong new evidence supporting the existence of a magnetic field with intensity of the order of 60 μT in the inner region of the solar nebula (~2-3 au), 2.0 ± 0.3 Myr after CAI formation. This field was stable over a timescale of at least ~0.5 Myr. The record of the solar nebula field provided by EC002 is particularly well resolved in time and represents one of the two earliest records so far measured. EC002's paleointensity estimate falls within the 95% confidence interval of the 34^{+36}_{-14}-μT paleointensity recorded by the chondrules of the LL chondrite Semarkona, 2.0 ± 0.8 Myr after CAI formation (Fig. 4) (13, 14). However, EC002's record offers a better spatial resolution compared to the record of Semarkona chondrules, given the uncertainties on their formation location, estimated at > 2 au (14). Moreover, EC002's record reflects a time-averaged magnetic field strength over a timescale of ~0.5 Myr, which contrasts with the near-instantaneous record of Semarkona chondrules that cooled over a timescale of hours (64). The fact that both paleointensities are compatible within uncertainties supports the conclusion drawn from numerical models that magnetic fields in the inner region of the nebula did not experience very significant changes (e.g., in direction) over short timescales (2).

The field intensity of 60 ± 18 μT recorded by EC002 at ~2-3 au is most compatible with an accretion rate of 10^{-8} $M_\odot$ yr^{-1}, if the vertical component of the field is aligned with the disk's rotation vector (2). On the other hand, such a field intensity is only compatible with

an accretion rate of ~10^{-6} $M_\odot$ yr^{-1} if both vectors are anti-aligned. This value of 10^{-6} $M_\odot$ yr^{-1} is two orders of magnitude faster than the average accretion rate derived from astronomical observations of extrasolar protoplanetary disks (5). Therefore, in agreement with the record of CO chondrules (15), our results provide a valuable constraint for dynamical models, as they largely favor the scenario where the vertical component of the field and the disk's rotation vector are aligned.

Materials and methods

The composition of the metal grains was determined using a Cameca SX Five electron microprobe at Université Pierre et Marie Curie Camparis facility (10 nA focused beam accelerated at 15 kV, counting time 30 s). All other experiments were conducted at the Centre Européen de Recherche et d'Enseignement des Géosciences de l'Environnement (CEREGE, France). EDS maps were obtained using a Hitachi S3000-N (15 kV) equipped with a Bruker X-ray X-Flash detector and a Spirit analyzer. Magneto-optical images were acquired following the method described in (65). The samples used for the paleomagnetic investigation were kept in a magnetically-shielded room (residual field ~500 nT) between 4 and 10 months before analysis. Low-field magnetic susceptibility (bulk, anisotropy and frequency-dependence) was measured on an Agico MFK1 with sensitivity of 5×10^{-13} m^3, operating at 200 A m^{-1} and 976 Hz (used to measure χ_{LF}) or 15,616 Hz. Calling k_1, k_2 and k_3 the eigenvalues of the matrix of anisotropy of susceptibility with $k_1 > k_2 > k_3$, the degree of anisotropy of susceptibility P is defined as k_1/k_3. The shape parameter T is defined as $[2\ln(k_2) - \ln(k_1) - \ln(k_3)]/[\ln(k_1) - \ln(k_3)]$ (66). IRM acquisition, hysteresis (M_s, M_{rs}, B_c) and DC backfield (B_{cr}) experiments were conducted on a Lake Shore Cryotronics 8600 Series vibrating sample magnetometer (VSM) with a sensitivity of ~1×10^{-9} A m^2. Hysteresis cycles were corrected for paramagnetic contribution by subtracting a linear regression slope calculated between 800 mT and 1 T. The FORC diagrams were obtained using the FORCinel software (38) and parameters: Sc0 = 6, Sb0 = 4, Sc1 = 8, Sb1 = 8, λ_H = 0.1, λ_U = 0.1. The remanence measurements and AF demagnetization were conducted on a SQUID cryogenic magnetometer (2G Enterprises, model 755R, sensitivity 1×10^{-11} A m^2), with an attached automatic AF 3-axis degausser system (maximum peak field 100 mT) in the magnetically-shielded room. The ARM was imparted using an AGICO AF demagnetizer and anhysteretic magnetizer (model LDA5). The SIRM was imparted using a 3-T pulse magnetizer from Magnetic Measurements. For thermal demagnetization, samples were heated in a controlled-atmosphere ASC Thermal Demagnetizer (model TD48). We followed the proportions proposed in (50) for each temperature step (Table S6). The VRM acquisition experiment was conducted over 380 days on a sample carrying its original NRM. The sample was subjected to a controlled magnetic field of 57 μT and its remanence was measured periodically. The VRM decay was quantified by storing the sample in a zero-field environment (< 50 nT) and monitoring the evolution of its remanence with time. Acquisition and decay rates are obtained by applying a linear regression to the remanence data as a function of log(time).

Acknowledgements

We thank two anonymous reviewers and the editors for their constructive assessment of the manuscript. We thank Jean Redelsperger for the loan of 11 individual stones of Erg

Chech 002 and Dr Jean-Alix Barrat for the loan of 2 additional samples. We also thank Prof Pierre Rochette for fruitful discussions of the results, Dr Minoru Uehara for assistance with the magneto-optical imaging, and Dr François Demory for assistance during the experiments. This project has received funding from the European Union's Horizon 2020 research and innovation programme under the Marie Skłodowska-Curie grant agreement No. 101027092.

Data availability: Data are available on the Zenodo repository with the DOI: 10.5281/zenodo.8187014.

References

1. Z.-Y. Li, *et al.*, "The earliest stages of star and planet formation: Core collapse, and the formation of disks and outflows" in *Protostars and Planets VI*, H. Beuther, R. S. Klessen, C. P. Dullemond, Eds. (University of Arizona Press, 2014), pp. 173–194.

2. B. P. Weiss, X.-N. Bai, R. R. Fu, History of the solar nebula from meteorite paleomagnetism. *Sci Adv* **7** (2021).

3. X.-N. Bai, Global Simulations of the Inner Regions of Protoplanetary Disks with Comprehensive Disk Microphysics. *ApJ* **845**, 75 (2017).

4. W. Béthune, G. Lesur, J. Ferreira, Global simulations of protoplanetary disks with net magnetic flux - I. Non-ideal MHD case. *Astron. Astrophys.* **600**, A75 (2017).

5. L. Hartmann, N. Calvet, E. Gullbring, P. Dïalessio, Accretion and the evolution of T Tauri disks. *Astrophys. J.* **495**, 385–400.

6. C. L. H. Hull, *et al.*, ALMA Observations of Polarization from Dust Scattering in the IM Lup Protoplanetary Disk. *ApJ* **860**, 82 (2018).

7. R. Brauer, S. Wolf, M. Flock, Magnetic fields in circumstellar disks - The potential of Zeeman observations. *Astron. Astrophys.* **607**, A104 (2017).

8. W. H. T. Vlemmings, *et al.*, Stringent limits on the magnetic field strength in the disc of TW Hya. *Astron. Astrophys.* **624**, L7 (2019).

9. P. H. Warren, Stable-isotopic anomalies and the accretionary assemblage of the Earth and Mars: A subordinate role for carbonaceous chondrites. *Earth Planet. Sci. Lett.* **311**, 93–100 (2011).

10. T. Kleine, *et al.*, The Non-carbonaceous–Carbonaceous Meteorite Dichotomy. *Space Sci. Rev.* **216**, 55 (2020).

11. S. J. Desch, A. Kalyaan, C. M. O'D. Alexander, The Effect of Jupiter's Formation on the Distribution of Refractory Elements and Inclusions in Meteorites. *ApJS* **238**, 11 (2018).

12. S. Sutton, *et al.*, The bulk valence state of Fe and the origin of water in chondrites. *Geochim. Cosmochim. Acta* **211**, 115–132 (2017).

13. R. R. Fu, *et al.*, Solar nebula magnetic fields recorded in the Semarkona meteorite. *Science* **346**, 1089–1092 (2014).

14. R. R. Fu, *et al.*, Implications for Chondrule Formation Regions and Solar Nebula Magnetism from Statistical Reanalysis of Chondrule Paleomagnetism. *Planet. Sci. J.* **4**, 151 (2023).

15. C. S. Borlina, *et al.*, Paleomagnetic evidence for a disk substructure in the early solar system. *Sci. Adv.* **7**, eabj6928 (2021).

16. L. Carporzen, *et al.*, Magnetic evidence for a partially differentiated carbonaceous chondrite parent body. *Proc. Natl. Acad. Sci. USA* **108**, 6386–6389 (2011).

17. R. R. Fu, *et al.*, The fine-scale magnetic history of the Allende meteorite: Implications for the structure of the solar nebula. *AGU Advances* **2** (2021).

18. C. Cournède, *et al.*, An early solar system magnetic field recorded in CM chondrites. *Earth Planet. Sci. Lett.* **410**, 62–74 (2015).

19. J. F. J. Bryson, B. P. Weiss, J. B. Biersteker, A. J. King, S. S. Russell, Constraints on the distances and timescales of solid migration in the early solar system from meteorite magnetism. *Astrophys J* **896**, 0–0 (2020).

20. J. Gattacceca, B. P. Weiss, M. Gounelle, New constraints on the magnetic history of the CV parent body and the solar nebula from the Kaba meteorite. *Earth Planet. Sci. Lett.* **455**, 166–175 (2016).

21. C. S. Borlina, B. P. Weiss, J. F. J. Bryson, P. J. Armitage, Lifetime of the outer solar system nebula from carbonaceous chondrites. *J. Geophys. Res. Planets* **127** (2022).

22. B. P. Weiss, *et al.*, A nonmagnetic differentiated early planetary body. *Earth Planet. Sci. Lett.* **468**, 119–132 (2017).

23. H. Wang, *et al.*, Lifetime of the solar nebula constrained by meteorite paleomagnetism. *Science* **355**, 623–627 (2017).

24. R. R. Fu, *et al.*, Weak magnetic fields in the outer solar nebula recorded in CR chondrites. *J. Geophys. Res. Planets* **125** (2020).

25. J. F. J. Bryson, B. P. Weiss, E. A. Lima, J. Gattacceca, W. S. Cassata, Evidence for asteroid scattering and distal solar system solids from meteorite paleomagnetism. *Astrophys J* **892**, 126 (2020).

26. J.-A. Barrat, *et al.*, A 4,565-My-old andesite from an extinct chondritic protoplanet. *Proc. Natl. Acad. Sci. U. S. A.* **118** (2021).

27. L. Fang, *et al.*, Half-life and initial Solar System abundance of 146Sm determined from the oldest andesitic meteorite. *Proc. Natl. Acad. Sci. U. S. A.* **119**, e2120933119 (2022).

28. A. Anand, P. M. Kruttasch, K. Mezger, 53Mn-53Cr chronology and ε54Cr-Δ17O genealogy of Erg Chech 002: the oldest andesite in the Solar System. *Meteorites and Planetary Sciences* (2023).

29. K. Zhu, *et al.*, Radiogenic chromium isotope evidence for the earliest planetary volcanism and crust formation in the Solar system. *Mon. Not. R. Astron. Soc. Lett.* **515**, L39–L44 (2022).

30. P. M. Reger, *et al.*, Al-Mg and U-Pb chronological records of Erg Chech 002 ungrouped achondrite meteorite. *Geochim. Cosmochim. Acta* **343**, 33–48 (2023).

31. A. Takenouchi, H. Sumino, A. Yamaguchi, J. A. Barrat, Noble gas chronology of Erg Chech 002 ungrouped achondrite in 84th Annual Meeting of the Meteoritical Society., (2021).

32. W. Neumann, R. Luther, M. Trieloff, P. M. Reger, A. Bouvier, Fitting Thermal Evolution Models to the Chronological Record of Erg Chech 002 and Modeling the Ejection Conditions of the Meteorite. *Planet. Sci. J.* **4**, 196 (2023).

33. D. J. Dunlop, Ö. Özdemir, *Rock Magnetism: Fundamentals and Frontiers*, D. Edwards, Ed. (Cambridge Univerty Press, 1997).

34. S.-C. L. L. Lappe, *et al.*, Mineral magnetism of dusty olivine: A credible recorder of pre-accretionary remanence. *Geochem. Geophys. Geosyst.* **12** (2011).

35. J. Shah, *et al.*, Long-lived magnetism on chondrite parent bodies. *Earth Planet. Sci. Lett.* **475**, 106–118 (2017).

36. P. Rochette, J. Gattacceca, Magnetic classification of stony meteorites: 3. Achondrites. *Met. Planet. Sci.* **44**, 405–427 (2009).

37. D. P. Maxbauer, J. M. Feinberg, D. L. Fox, MAX UnMix: A web application for unmixing magnetic coercivity distributions. *Comput. Geosci.* **95**, 140–145 (2016).

38. R. J. Harrison, J. M. Feinberg, FORCinel: An improved algorithm for calculating first-order reversal curve distributions using locally weighted regression smoothing. *Geochem. Geophys. Geosyst.* **9** (2008).

39. R. J. Harrison, *et al.*, Simulation of remanent, transient, and induced FORC diagrams for interacting particles with uniaxial, cubic, and hexagonal anisotropy. *J. Geophys. Res. [Solid Earth]* **124**, 12404–12429 (2019).

40. R. Egli, “Magnetic Characterization of Geologic Materials with First-Order Reversal Curves” in *Magnetic Measurement Techniques for Materials Characterization*, V.

Franco, B. Dodrill, Eds. (Springer International Publishing, 2021), pp. 455–604.

41. L. Nagy, *et al.*, Stability of equidimensional pseudo-single-domain magnetite over billion-year timescales. *Proc. Natl. Acad. Sci. U. S. A.* **114**, 10356–10360 (2017).

42. F. Vervelidou, B. P. Weiss, F. Lagroix, Hand magnets and the destruction of ancient meteorite magnetism. *J. Geophys. Res. Planets* **128** (2023).

43. L. Néel, Théorie du traînage magnétique des ferromagnétiques en grains fins avec application aux terres cuites. *Annal. Géophys.* **5**, 99–136 (1949).

44. B. M. Moskowitz, Magnetic viscosity, diffusion after-effect, and disaccommodation in natural and synthetic samples. *Geophys. J. Int.* **82**, 143–161 (1985).

45. T. A. J. Jull, "Terrestrial ages of meteorites" in *Accretion of Extraterrestrial Matter Throughout Earth's History*, (2001), pp. 241–266.

46. J. L. Kirschvink, The least-squares line and plane and the analysis of palaeomagnetic data. *Geophys. J. Int.* **62**, 699–718 (1980).

47. L. Tauxe, H. Staudigel, Strength of the geomagnetic field in the Cretaceous Normal Superchron: New data from submarine basaltic glass of the Troodos Ophiolite. *Geochem. Geophys. Geosyst.* **5** (2004).

48. D. W. Sears, Temperature gradients in meteorites produced by heating during atmospheric passage. *Modern Geol.* **5**, 155–164 (1975).

49. M. Sato, N. L. Hickling, J. E. McLane, Oxygen fugacity values of Apollo 12, 14, and 15 lunar samples and reduced state of lunar magmas in *Proc. Lunar Planet. Sci. Conf.*, 4., pp. 1061–1079.

50. C. Suavet, B. P. Weiss, T. L. Grove, Controlled-atmosphere thermal demagnetization and paleointensity analyses of extraterrestrial rocks. *Geochem. Geophys. Geosyst.* **15**, 2733–2743 (2014).

51. C. Cournède, I. Garrick-Bethell, R. S. Coe, M. Le Goff, Y. Gallet, Mineralogical changes upon heating in the Millbillillie meteorite: Implications for paleointensity determination in Apollo samples. *C. R. Geosci.* **348**, 551–560 (2016).

52. M. Uehara, J. Gattacceca, P. Rochette, F. Demory, E. M. Valenzuela, Magnetic study of meteorites recovered in the Atacama desert (Chile): Implications for meteorite paleomagnetism and the stability of hot desert surfaces. *Phys. Earth Planet. Inter.* **200–201**, 113–123 (2012).

53. P. A. Bland, *et al.*, Climate and rock weathering: a study of terrestrial age dated ordinary chondritic meteorites from hot desert regions. *Geochim. Cosmochim. Acta* **62**, 3169–3184 (1998).

54. D. E. Watson, E. E. Larson, R. L. Reynolds, Microscopic and thermomagnetic analysis of Apollo 17 breccia and basalt: Feasibility of obtaining meaningful paleointensities of the lunar magnetic field in *Proc. Lunar Planet. Sci. Conf.*, 5., (1974), pp. 827–829.

55. E. E. Larson, Degradation of lunar basalts during thermal heating in vacuum and its relation to paleointensity measurements in *Lunar Planet. Sci. Conf.*, 9., (1978), p. 633.

56. Ö. Özdemir, D. J. Dunlop, Crystallization remanent magnetization during the transformation of maghemite to hematite. *J. Geophys. Res.* **93**, 6530 (1988).

57. Y. Yu, L. Tauxe, A. Genevey, Toward an optimal geomagnetic field intensity determination technique. *Geochem. Geophys. Geosyst.* **5** (2004).

58. A. Stephenson, D. W. Collinson, Lunar magnetic field palaeointensities determined by an anhysteretic remanent magnetization method. *Earth Planet. Sci. Lett.* **23**, 220–228 (1974).

59. J. Gattacceca, P. Rochette, Toward a robust normalized magnetic paleointensity method applied to meteorites. *Earth Planet. Sci. Lett.* **227**, 377–393 (2004).

60. B. P. Weiss, S. M. Tikoo, The lunar dynamo. *Science* **346**, 1246753 (2014).

61. K. H. Dodds, J. F. J. Bryson, J. A. Neufeld, R. J. Harrison, The thermal evolution of planetesimals during accretion and differentiation: Consequences for dynamo generation by thermally-driven convection. *J. Geophys. Res. Planets* **126** (2021).

62. B. P. Weiss, *et al.*, Magnetism on the Angrite parent body and the early differentiation of planetesimals. *Science* **322**, 713–716 (2008).

63. R. Oran, B. P. Weiss, O. Cohen, Were chondrites magnetized by the early solar wind? *Earth Planet. Sci. Lett.* **492**, 222–231 (2018).

64. R. H. Jones, J. Villeneuve, G. Libourel, “Thermal Histories of Chondrules” in *Chondrules: Records of Protoplanetary Disk Processes*, (Cambridge University Press, 2018), pp. 57–90.

65. M. Uehara, C. J. van der Beek, J. Gattacceca, V. A. Skidanov, Y. Quesnel, Advances in magneto-optical imaging applied to rock magnetism and paleomagnetism. *Geochem. Geophys. Geosyst.* **11**, Q05Y09 (2010).

66. V. Jelinek, Characterization of the magnetic fabric of rocks. *Tectonophysics* **79**, T63–T67 (1981).